Energy dissipation in electrosprays and the geometric scaling of the transition region of cone–jets

M. GAMERO-CASTAÑO†

Department of Mechanical and Aerospace Engineering, University of California, Irvine, CA 92697, USA

The characterization of electrosprayed droplets by means of retarding potential and time-of-flight techniques yields relevant information on the physics of the cone–jet itself. The experimental data reveal that a significant fraction of the electric power injected in the cone–jet is degraded by ohmic and viscous dissipations, as well as converted into surface energy. The degradation of energy can be cast in the form of a measurable voltage deficit that depends on the fluid's viscosity, electrical conductivity and dielectric constant, but is independent of its flow rate. These experimental facts require an identical scaling r_t for both the characteristic radial and axial lengths of the cone-to-jet transition, the region where conduction current is transformed into convected surface charge. This fundamental scale is the geometric mean of the electrical relaxation length and the distance from the Taylor cone apex where the dynamic and capillary pressures become comparable. These two lengths are of the same order in a wide range of operational conditions, which further confirms the importance of the role played by electrical relaxation phenomena in the physics of cone–jets. The validity of r_t is further supported by the numerical results of Higuera (*J. Fluid Mech.*, vol. 484, 2003, pp. 303–327), whose profiles of the transition region non-dimensionalized with r_t remain unchanged when the flow rate is varied. Finally, the dissipation of energy significantly increases the temperature of fluids with high conductivities, and future models for the cone–jets of these liquids will need to account for thermal effects.

Key words: capillary flows, electrohydrodynamic effects, MHD and electrohydrodynamics

1. Introduction

Electrospraying is an atomization technique with a singular ability for producing uniform sprays of droplets with diameters as small as a few tens of nanometres. In a typical experimental configuration, a liquid is fed to the tip of a capillary electrode held at high potential. The liquid then shapes into a conical meniscus issuing a slender jet, which eventually becomes unstable and breaks into charged droplets. These capillary-supported electrosprays were first systematically investigated by Zeleny (1914), and the conical shape of the liquid meniscus was explained by Taylor (1964). Although electrosprays can operate in a variety of regimes (Cloupeau & Prunet-Foch 1990),

† Email address for correspondence: mgameroc@uci.edu

the so-called cone–jet mode (Cloupeau & Prunet-Foch 1989), characterized by the formation of a steady jet, is of special interest and has been studied in great detail (Fernández de la Mora 2007).

The generation of submicrometre-sized fluid structures is arguably the most interesting feature of cone–jets. It is well suited for technological applications such as electrospray mass spectrometry (Fenn *et al.* 1989), the encapsulation of drugs (Loscertales *et al.* 2002), nanodroplet sputtering (Gamero-Castaño & Mahadevan 2009), combustion (Kyritsis *et al.* 2004), space propulsion (Gamero-Castaño & Hruby 2001), etc. It also provides an interesting area of research on free surfaces, with length scales that can approach molecular dimensions and strong couplings between hydrodynamics and electrical phenomena. The various theories for explaining the behaviour of cone–jets generally consider three sequential regions: a static cone in which ohmic conduction is the dominant current mechanism; a transition region between the cone and the emerging jet where conduction current injects charge on the surface of the liquid and progressively becomes surface current (i.e. convected surface charge); and a jet accelerated by electrical forces and where surface current is the dominant form of charge transport. The analysis of the cone-to-jet transition is the central problem in these theories because the current and the diameter of the base of the jet are fixed in this region, controlled by local parameters largely insensitive to the variations of the geometry and electrostatics in the far field. For example, Fernández de la Mora & Loscertales (1994) were able to explain the experimental current law by considering a transition region dominated by electrical relaxation phenomena. In contrast, Gañán-Calvo *et al.* (1996) and Gañán-Calvo (2004) inferred that the surface charge is in equilibrium throughout the cone–jet, and obtained alternative scaling laws for the current and jet diameter based on this idea. Gañán-Calvo (1997) has also analysed the jet by coupling its dynamics with the electric field induced by the Taylor cone, an idea that makes it possible to formulate a local model of the transition region with asymptotic, far-field boundary conditions. Higuera (2003) has integrated the complete set of partial differential equations for the transition region and has also studied several asymptotic limits. Finally, the work of Collins *et al.* (2008), who solve the complete set of equations in the cone–jet and surrounding electrostatic domain, is a departure from the models centred in the transition region. Common to all cone–jet theories is the use of simplifying hypotheses and the need to validate them with experimental results.

The electric current and the droplet diameter are the parameters more commonly measured and used to support electrospray models. The current is fixed in the transition region and can be determined easily. However, the two opposite hypotheses regarding charge relaxation yield a similar current law for most cone–jets (Fernández de la Mora & Loscertales 1994; Gañán-Calvo 1997), and therefore the comparison between measured and predicted values cannot clarify which point of view is correct. A validation based on the droplet diameter is equally inconclusive, because this parameter is determined by the jet dynamics and its inherently random breakup, and therefore does not directly relate to the physics of the transition region. This problem is compounded by the natural distribution of droplet sizes and the difficulty of measuring droplet diameters with the accuracy required to distinguish between relatively similar scaling laws (Fernández de la Mora & Loscertales 1994; Gañán-Calvo 1997). The need for new measurements able to yield discriminating information directly connected to the transition region is hence clear and provides one motivation for the present study.

Cone–jets may be probed through measurements carried out at reduced pressure or in a vacuum, and there is a long tradition of doing so in the so-called electrohydrodynamic ionization (Cook 1986). The current can then be investigated very much as under atmospheric pressure, and this has shown that the background gas and the space-charge effects associated with the transport of charged drops through the gas have negligible effects on the characteristics of the jet (Gamero-Castaño *et al.* 1998). Furthermore, in a vacuum, the sum of the potential and kinetic energy of a drop is conserved following its release from the jet, and may hence be measured in the form of the voltage ϕ_S required to stop their flow to a collecting electrode. This stopping voltage is generally smaller than the voltage ϕ_E applied to the electrode supporting the cone–jet, so that the difference $\Delta = \phi_E - \phi_S$ may be interpreted as the voltage deficit or irreversible loss of energy (per unit charge) needed to form the drop. For the case of liquid metals, energy analysis of the ejected ions has shown that there is no measurable voltage drop involved in the formation of the jet (Prewett & Mair 1991). But the situation is quite different for electrolytes, where the finite electrical resistance of the liquid is a key factor controlling the jet dynamics. Indeed, Huberman's (1970) pioneering stopping potential study with glycerol indicated that, in this case, there is a substantial voltage deficit. Because the voltage deficit is in principle a computable quantity, its systematic measurement should shed new light on the physics of cone–jets and provide a reference to test the various theories.

This study focuses on the determination of the voltage deficit of cone–jets and its relationship with the physics of the transition region, and is organized as follows. Section 2 presents the properties of the studied liquids, a description of the experimental set-up with focus on the retarding potential analysers and an induction charge detector (ICD) for characterizing individual drops, and electrospray current data. Section 3.1 introduces the retarding potential measurements and establishes a link between the voltage drop, the dissipation of energy and the generation of surface energy in the cone–jet. Section 3.2 rationalizes the spread of the retarding potential distributions. Section 3.3 presents the remarkable independence between the voltage deficit and the flow rate, establishes the functional dependence of the voltage deficit via dimensional analysis and demonstrates that the dissipation of energy is responsible for the largest fraction of the voltage deficit. Section 3.4 derives the geometric scaling of the transition region and discusses the implications of this scale on the physics of cone–jets. Finally, the main results of this study are summarized in §4.

2. Experimental

Figure 1(*a*) is a sketch of the experimental set-up. The liquid to be electrosprayed is held in a glass reservoir and fed into a vacuum chamber through a capillary tube. The pressure inside the reservoir driving the liquid flow rate Q is monitored and controlled with a vacuum pump, compressed nitrogen and a transducer. The emitter and the feeding line are made of a single stainless-steel tube with inner and outer diameters of 100 and 220 μm. A voltage difference between the emitter and a facing extractor is applied to form a cone–jet. The resulting charged drops exit the emitter and extractor regions through a small orifice perforated in the extractor, and enter an area where they are analysed by several detectors. A background pressure of 10^{-6} Torr is sustained with a combination of turbomolecular and mechanical pumps. The mean free path of nitrogen molecules at this pressure and ambient temperature is approximately 50 m, and therefore a drop's loss of kinetic energy due to collisions
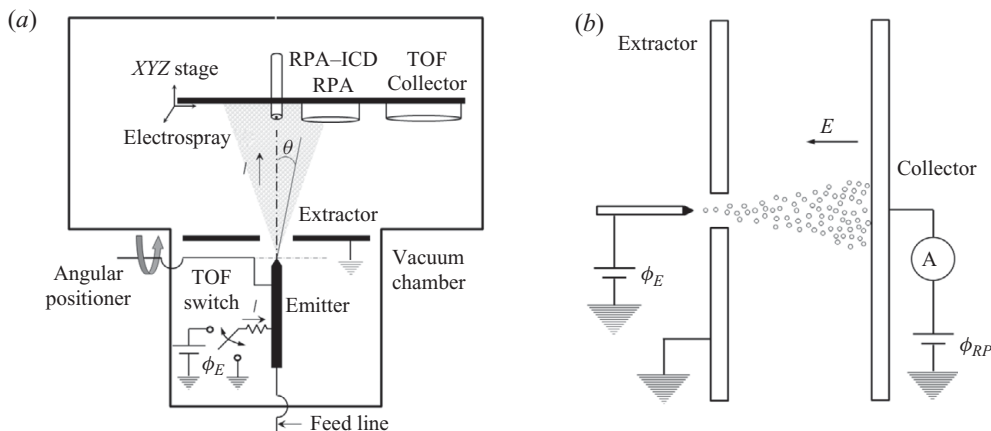
FIGURE 1. (*a*) Experimental set-up. Liquid solutions are electrosprayed in a vacuum, producing charged droplets that are characterized with retarding potential and time-of-flight detectors. (*b*) Cumulative retarding potential analyser. The beam current reaching the collector is measured as a function of the retarding potential.

with the background gas is negligible. The entire electrospray beam is characterized with a time-of-flight detector and a cumulative retarding potential analyser. The time-of-flight (TOF) detector has been described in detail elsewhere, and is mainly used to measure the mass flow rate of the electrospray (Gamero-Castaño & Hruby 2001). The cumulative retarding potential analyser is shown in figure 1(*b*): the planar electric field between the grounded extractor and a facing collector can be made large enough to turn the incoming flux of charged droplets, and the current striking the collector is measured with an electrometer as a function of the retarding potential. A droplet with a velocity vector in the direction of the electric field is sensed by the electrometer if and only if its stopping potential ϕ_S is larger than the potential of the collecting electrode ϕ_{RP}. The stopping potential of a droplet is the sum of its kinetic and potential energies divided by its charge, and therefore is a constant of motion in a stationary electric field:

$$\phi_S = \frac{m}{q}\frac{v^2(\boldsymbol{x})}{2} + \phi(\boldsymbol{x}) = \text{constant}. \qquad (2.1)$$

Droplets entering the gap at an angle θ with the electric field require a smaller retarding potential to prevent collection:

$$\phi_{RP} = \cos^2(\theta)\phi_S. \qquad (2.2)$$

The electrospray beams are conical, and therefore the detector in figure 1(*b*) produces retarding potential distributions with an artificial tail at low retarding potentials. This error increases with the current (the higher the current, the larger the beam angle) and is relatively small for these narrow beams.

We have also measured the stopping potential, charge and diameter of individual droplets with a differential retarding potential analyser and an ICD operating in tandem (Gamero-Castaño 2009). The spectrometer is sketched in figure 2(*a*). The droplets exit the extractor with radial trajectories, making it possible to sample drops at different polar angles by rotating the emitter. A charged droplet enters the retarding potential analyser (essentially an electrostatic mirror) through a small orifice, and its path is deflected by a planar and homogeneous electric field. The
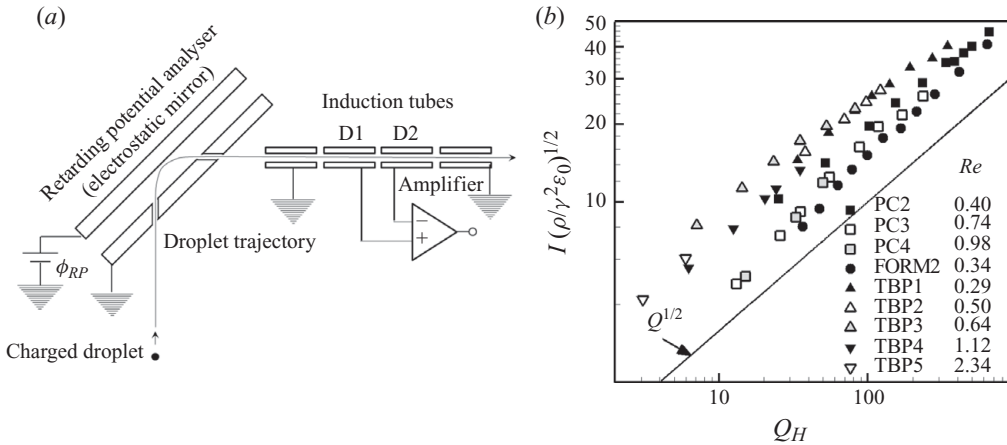
FIGURE 2. (*a*) Differential retarding potential analyser and ICD. When operating in tandem, this combination yields the retarding potential, charge and diameter of individual droplets. (*b*) Experimental values of the dimensionless electrospray current and flow rate Q_H. The current exhibits the typical $Q_H^{1/2}$ law and also depends on the dielectric constant.

geometry of the electrodes is such that the droplet exits the mirror through a second orifice when its stopping potential coincides with the potential difference between the plates. The exit orifice is aligned with the four tubular electrodes of the ICD, and the droplet induces an electric potential proportional to its charge on two of them as it flies through. The potential difference between these tubes is amplified, generating a one-period rectangular wave from which the droplet's charge and time of flight are measured. The time-of-flight measurement combined with the known stopping potential yields the droplet's charge-to-mass ratio, while the mass is obtained from this parameter and the charge measurement; the droplet diameter is computed from the mass and the liquid density (Gamero-Castaño 2009). We also measure stopping-potential distributions with the electrostatic mirror, using a second pair of orifices 10 mm above those aligned with the ICD. The droplets exiting the mirror impinge on a collecting electrode where the current is recorded as a function of the retarding potential.

The need to work in vacuum requires liquids with low vapour pressure to minimize evaporation losses. It is important to cover a wide range of electrical conductivities, a physical parameter with a strong influence on the cone–jet and which can be made to span orders of magnitude by varying the concentration of dissolved electrolytes. We have studied solutions based on propylene carbonate, formamide and tributyl phosphate, all of which are highly involatile and moderately viscous. Tributyl phosphate solutions with different conductivities were made by adding small concentrations of the salt tetrabutylammonium tetraphenylborate, or the ionic liquid EmiIm (McEwen *et al.* 1999). Likewise, propylene carbonate and formamide solutions were formulated with different concentrations of the EmiIm solute. Table 1 lists the electrical conductivity K of the solutions investigated in this paper. Their densities ρ, surface tensions γ, viscosities μ, heat capacities c and dielectric constants ε are assumed to be those of the pure solvents and given in table 2 (Riddick, Bunger & Sakano 1986).

Figure 2(*b*) shows the basic electrospray current data scaled with $(\gamma^2 \varepsilon_0 / \rho)^{1/2}$, as a function of the dimensionless flow rate Q_H, for most solutions in table 1. Any cone–jet

Solution	PC1	PC2	PC3	PC4	FORM1	FORM2
K (S m^{-1})	0.121	0.0142	2.23×10^{-3}	9.47×10^{-4}	0.104	0.0161
Δ (V)	217	245	340	390	270	320
Solution	TBP1	TBP2	TBP3	TBP4	TBP5	TBP6
K (S m^{-1})	5.8×10^{-3}	1.1×10^{-3}	5.32×10^{-4}	1.0×10^{-4}	1.1×10^{-5}	4.1×10^{-6}
Δ (V)	131	185	210	307	520	754

TABLE 1. Electrical conductivity and total voltage deficit of the propylene carbonate (PC), formamide (FORM) and tributyl phosphate (TBP) solutions characterized in this study.

Solvent	ρ (Kg m^{-3})	γ (N m^{-1})	μ (Pa s)	c (J (Kg K)$^{-1}$)	ε
PC	1200	0.0419	0.00276	1210 (25 °C)	64.9 (25 °C)
FORM	1133	0.0583	0.00376	2390 (25 °C)	111
TBP	976 (25 °C)	0.0275	0.00339 (25 °C)		8.91 (25 °C)

TABLE 2. Density, surface tension, viscosity, specific heat capacity and dielectric constant of propylene carbonate, formamide and tributyl phosphate. Unless otherwise specified, the values are for a temperature of 20 °C.

variable, made dimensionless with the appropriate scale, is a function of at most three dimensionless groups (Higuera 2003). The parameters ρ, γ, K and the permittivity of the vacuum ε_0 are generally employed to define scales, while the dielectric constant, the dimensionless flow rate and the Reynolds number,

$$Q_H = \frac{\rho K Q}{\gamma \varepsilon_0}, \quad Re = \frac{\rho^{1/3} \varepsilon_0^{1/3} \gamma^{2/3}}{\mu K^{1/3}}, \quad (2.3)$$

are the common choices for independent dimensionless groups. Fernández de la Mora & Loscertales (1994) have also used the alternative dimensionless flow rate $Q_{FM} = \rho K Q / (\gamma \varepsilon \varepsilon_0)$.

The data in figure 2(*b*) approximately follow a $Q_H^{1/2}$ law, as predicted by the theories of Fernández de la Mora and Gañán-Calvo (2004). At fixed Q_H, the current diminishes with increasing dielectric constant, which is compatible only with Fernández de la Mora's scaling. Our data also compare well with the values computed by Higuera (2003) for the dielectric constants 5 and 50. For example, we measure dimensionless currents of 5.14 and 7.8 for PC4 at $Q_H = 15.3$ ($\varepsilon = 64.9$, $Re = 0.98$), and TBP4 at $Q_H = 12.5$ ($\varepsilon = 8.91$, $Re = 1.12$). Higuera reports a current of 5.42 for $Q_H = 15.3$, $\varepsilon = 50$ and $Re = 1$ (a point similar to PC4's) and a value of 8.60 for $Q_H = 12.5$, $\varepsilon = 5$ and $Re = 1$ (a point similar to TBP4's). More generally, the current computed by Higuera increases with decreasing dielectric constant, and our figure confirms that this trend continues at much higher flow rates. (Higuera studies only dimensionless flow rates smaller than 20.)

Before moving to the retarding potential investigation, we would like to emphasize the extent of the operational range characterized in this study. For example, the electrical conductivity and the dielectric constant have been varied by factors of 3.0×10^4 and 12.5, while the flow rates for almost every solution start near the minimum value and end at the onset of lateral oscillations in the jet (Rosell-Llompart & Fernández de la Mora 1994).

θ (deg.)	$\langle D \rangle$ (μm)	$\sigma_D/\langle D \rangle$ (%)	$\langle q \rangle$ (C)	$\sigma_q/\langle q \rangle$ (%)	$\langle \xi \rangle$ (C kg^{-1})	$\sigma_\xi/\langle \xi \rangle$ (%)
0	0.931	7.60	2.70×10^{-15}	21.8	5.59	4.61
4	0.871	6.64	2.23×10^{-15}	19.1	5.65	5.30
6	0.824	6.07	1.88×10^{-15}	16.9	5.65	6.92
8	0.754	5.77	1.44×10^{-15}	15.1	5.70	8.62

TABLE 3. Average and relative standard deviation of the diameter, charge and charge-to-mass ratio of PC3 droplets for a 4.9×10^{-12} m s^{-3} flow rate (33 nA electrospray current) and four different polar angles. The drops are sampled in the full range of stopping potentials.
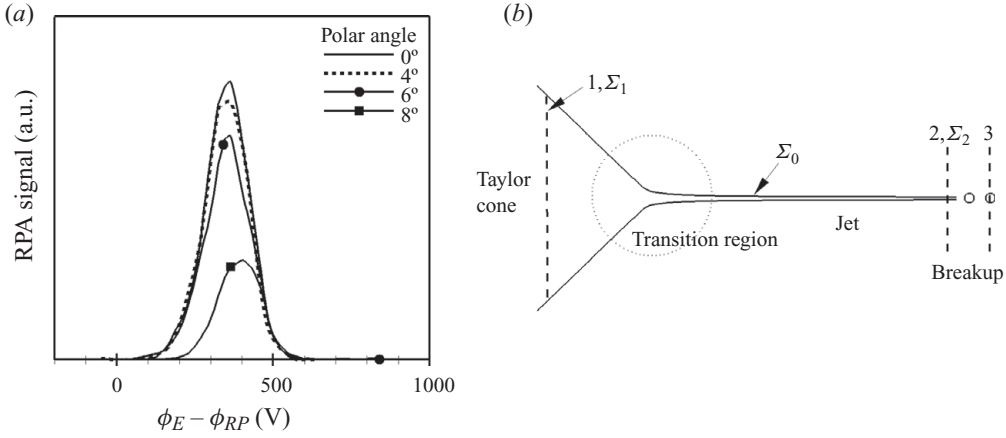

FIGURE 3. (*a*) Emitter potential minus drop's retarding potential spectra of a PC3 electrospray ($I = 33$ nA), measured at four different polar angles with the differential retarding potential analyser. The droplets have a significant voltage deficit due to the dissipation of energy and the generation of surface in the cone–jet. (*b*) Sketch of the cone–jet.

3. Discussion

3.1. *The stopping potential of a droplet and its correlation with cone–jet parameters*

Figure 3(*a*) shows typical stopping potential distributions for a PC3 beam with a flow rate of 4.9×10^{-12} m s^{-3} and a current of 33 nA. The distributions are measured with the differential retarding potential analyser at four different polar angles. (The envelope of the beam has an angle of $9°$.) The averages and standard deviations of the droplets' diameter, charge and charge-to-mass ratio are given in table 3. The abscissa of figure 3(*a*) is the potential of the emitter (2040 V) minus the retarding potential, and therefore may be regarded as the voltage deficit of the drops. The average deficit of 350 V suggests that 17 % of the electrical power transferred to the electrospray is degraded in the cone–jet and not converted into beam kinetic power. The goal of this section is to correlate this potential deficit with hydrodynamic parameters in the cone–jet. For simplicity, we will first examine an ideal breakup producing identical droplets, while the complexities associated with the distributions of droplets' charges and diameters will be analysed in § 3.2.

Let us consider the idealized geometry of an electrospray depicted in figure 3(*b*), which includes the Taylor cone, a transition region, the jet, the jet breakup and emitted droplets. The surfaces Σ_1 and Σ_2 are the intersections of $r\theta$ planes with the cone–jet far upstream and near the jet breakup, while Σ_0 is the surface of revolution. The following expression can be derived by integrating the equation of mechanical energy

over the volume Π enclosed by the three surfaces (see derivation in the supplementary online material, available at journals.cambridge.org/flm):

$$\left(\frac{v_2^2}{2} + \frac{p_2}{\rho}\right) - \left(\frac{v_1^2}{2} + \frac{p_1}{\rho}\right) = \frac{I}{\rho Q}(\phi_1 - \phi_2) - \frac{P_\Omega + P_\mu}{\rho Q}, \tag{3.1}$$

where ϕ is the electric potential, v and p are the fluid's velocity and pressure, and P_Ω and P_μ are the total ohmic and viscous powers dissipated in the cone–jet,

$$P_\Omega = \int_\Pi \boldsymbol{E} \cdot \boldsymbol{J} \, \mathrm{d}V, \qquad P_\mu = \int_\Pi \boldsymbol{\tau}_\mu : \nabla \boldsymbol{v} \, \mathrm{d}V, \tag{3.2}$$

where $\boldsymbol{E}$, $\boldsymbol{J}$ and $\boldsymbol{\tau}_\mu$ stand for the electric field, the conduction current density in the liquid bulk and the viscous stress tensor. The electrical power $I(\phi_1 - \phi_2)$ transferred to the cone–jet is partially converted into mechanical energy and partially degraded by viscous and ohmic dissipations (which in turn increase the internal energy and the temperature of the fluid). The specific kinetic energy and the pressure decay very fast upstream of the transition region because of the increasing cross-section of the Taylor cone, and therefore the term in the second bracket in (3.1) can be neglected. We next assume that the periodic breakup takes place within a short distance, so that the potential difference between the emitted drops and the jet is negligible, $\phi_2 \cong \phi_3$. Conservation of charge and mass then requires the charge-to-mass ratio ξ of the drops to be that of the fluid in the jet ξ_J, while conservation of momentum requires a velocity jump:

$$\xi = \xi_J, \quad v_2 - v_3 = \frac{2\pi R_2 \gamma}{\rho Q} - \frac{\pi R_2^2 p_2}{\rho Q} = v_2 \left(\frac{2\gamma}{\rho v_2^2 R_2} - \frac{p_2}{\rho v_2^2}\right), \tag{3.3}$$

where $R(z)$ stands for the radius of the jet. The jump in velocities is a function of jet variables only and is a small fraction of the velocity because at Σ_2 the capillary pressure is significantly smaller than the dynamic pressure. We now use (3.3) and $\phi_2 = \phi_3$ to express the stopping potential of the droplets in terms of jet variables,

$$\phi_S = \frac{v_3^2}{2\xi_J} + \phi_3 = \frac{1}{2\xi_J}\left(v_2 - \frac{2\pi R_2 \gamma}{\rho Q} + \frac{\pi R_2^2 p_2}{\rho Q}\right)^2 + \phi_2, \tag{3.4}$$

and $\xi_J = I/(\rho Q)$ and (3.1) to obtain

$$\phi_S = \phi_1 - \frac{P_\Omega + P_\mu}{I} - \frac{2Q\gamma}{IR_2} + \frac{Q}{I}\frac{2}{\rho v_2^2}\left(\frac{\gamma}{R_2} - \frac{p_2}{2}\right)^2. \tag{3.5}$$

Since the capillary pressure is significantly smaller than the dynamic pressure, the fourth term on the right-hand side can be neglected with respect to the third one. This finally yields the equation for the voltage deficit Δ:

$$\Delta = \Delta_\Omega + \Delta_\mu + \Delta_\gamma, \tag{3.6}$$

$$\Delta = \phi_1 - \phi_S, \quad \Delta_\Omega = \frac{P_\Omega}{I}, \quad \Delta_\mu = \frac{P_\mu}{I}, \quad \Delta_\gamma = \frac{2Q\gamma}{IR_2}. \tag{3.7}$$

The voltage deficit results from the degradation of mechanical and electrical energy by dissipative processes, together with the generation of surface. ($2Q\gamma/IR_2$ is the flux of surface energy across Σ_2, divided by the electrospray current.) Although, for convenience, in the narrative we will refer to Δ, Δ_Ω, Δ_μ and Δ_γ as the total, ohmic, viscous and surface voltage deficits, none of these terms should be confused with a difference of electric potentials between two points.
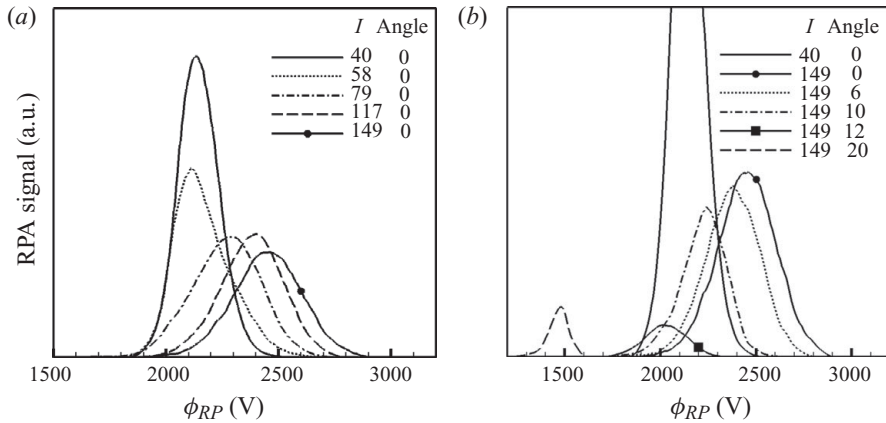
FIGURE 4. Retarding potential distributions for FORM2 obtained with the electrostatic mirror. (*a*) Spectra associated with main droplets at the beam axis and for different flow rates. (*b*) Spectra for a high flow rate ($I = 149$ nA) recorded throughout the beam angular range. All the spectra are for main droplets, except the one at 20° which is for satellites.

3.2. *The broadening of the retarding potential distribution*

The structure and complexity of the sprays produced by cone–jets vary with the flow rate. Most cone–jets operating at or near the minimum flow rate only produce main droplets with relatively narrow diameter and charge-to-mass-ratio distributions (see table 3). As the flow rate increases, a critical point is reached that triggers the formation of satellite droplets and increasing numbers of them are generated thereafter (Ashgriz & Mashayek 1995). Satellite droplets result from the detachment of the fluid ligament connecting two main droplets, and are smaller and have a higher charge-to-mass ratio (López-Herrera & Gañán-Calvo 2004; Collins, Harris & Basaran 2007). When satellite droplets are produced the charge-to-mass-ratio distribution of the main drops broadens, because those yielding satellites lose more charge than mass to them, while those that do not retain a charge-to-mass ratio similar to that of the jet. If the flow rate is further increased, a second critical point is reached at which the jet becomes susceptible to sinusoidal perturbations, oscillates and generates droplets in a much broader diameter distribution lacking distinct droplet families. This phenomenology is best observed with time-of-flight spectrometry (Gamero-Castaño & Hruby 2002; Gamero-Castaño 2008) and is also evident in the retarding potential curves: satellite and main droplets have two distinct, separate ranges of stopping potentials; the standard deviation of main droplets is smallest for breakups producing only main droplets and increases when satellites are generated; and the maximum retarding potential of main droplets increases with the flow rate, while their minimum retarding potential remains constant. We illustrate this in figure 4 with spectra for FORM2. Figure 4(*a*) shows retarding potential distributions of main droplets at different flow rates, sampled in the beam axis. The potential of the emitter is 2420 V. The two spectra for the lowest currents are similar; satellite droplets start to appear near a current of 67 nA, and from this point forward, the main droplet distributions become noticeable broader and shift to larger voltage values. Figure 4(*b*) shows distributions for the higher flow rate at different polar angles and that of the lowest flow rate as a reference. It is known that when the two populations of droplets are present in the same spray they separate into two coaxial beams, the satellites surrounding the main droplets (Gamero-Castaño 2008). Thus, in the case of the 149 nA electrospray,
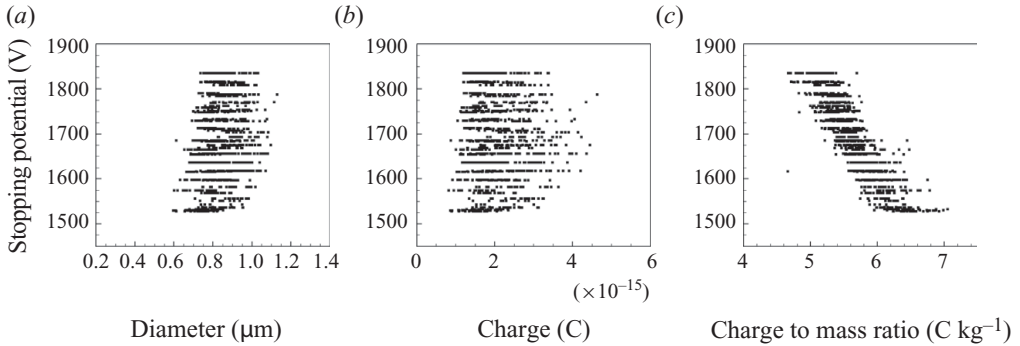
FIGURE 5. Stopping potential of individual droplets versus diameter, charge and charge-to-mass ratio. The stopping potential is well correlated with the charge-to-mass ratio. The graphs contain data for 1195 droplets sampled from the PC3 spray of figure 3(*a*).

the satellite drops only appear at angles larger than 16°, while main droplets are only detected at angles smaller than 13°. Figure 4(*b*) shows that the satellite drops (the spectrum at a 20° angle) have stopping potentials significantly smaller than, and separated from, those of main drops. A weaker angular segregation also occurs within the main droplet population, with higher charge-to-mass ratios and lower retarding potentials predominantly appearing at increasing angle. It is worth noting that the main droplets of the 149 nA electrospray with smaller stopping potential (those at a 12° angle) have a distribution engulfed by that of the 40 nA electrospray, despite the two flow rates being separated by a ratio of 8.1. This clustering occurs for all flow rates and solutions characterized in this study. Thus, it is apparent that the maximum stopping potential of main drops increases with the flow rate, but their minimum stopping potential is constant and equal for all flow rates. The significance of this observation will be discussed in § 3.3.

Understanding what causes the spread of retarding potentials is important because a value from the distribution needs to be chosen as Δ. The correlation between the stopping potentials of droplets and their various diameters, charges and charge-to-mass ratios is the likely origin of the spread, a hypothesis that we test in the next set of plots. Figure 5 shows the retarding potential versus the diameter, charge and charge-to-mass ratio of 1195 droplets for the PC3 electrospray in figure 3(*a*) and table 3. The retarding potential clearly depends on the charge-to-mass ratio (the Pearson's correlation coefficient is $\rho_{\phi\xi} = -0.82$), it does not depend on the charge ($\rho_{\phi q} = 0.018$), and exhibits a moderate correlation with the diameter ($\rho_{\phi D} = 0.21$). The latter is probably due to the correlation between diameter and charge-to-mass ratio, $\rho_{D\xi} = -0.22$. The negative correlation between a drop's charge-to-mass ratio and its retarding potential is explained by the kinetic energy gained by the fluid in the jet, coupled with the natural distribution of charge-to-mass ratios induced by the random breakup. This is better illustrated by neglecting the small variations of the potential and velocity in the breakup,

$$\phi_S = \frac{v_3^2}{2\xi} + \phi_3 \cong \frac{v_2^2}{2\xi} + \phi_2 = \frac{\xi_J}{\xi}(\phi_{SJ} - \phi_2) + \phi_2, \tag{3.8}$$

where ϕ_{SJ} is the stopping potential of the fluid in the jet. In a breakup with a stationary location, ϕ_{SJ} and ϕ_2 are constant, and the retarding potential of a droplet is proportional to the ratio ξ_J/ξ. Hence, the higher the droplet's charge-to-mass ratio,
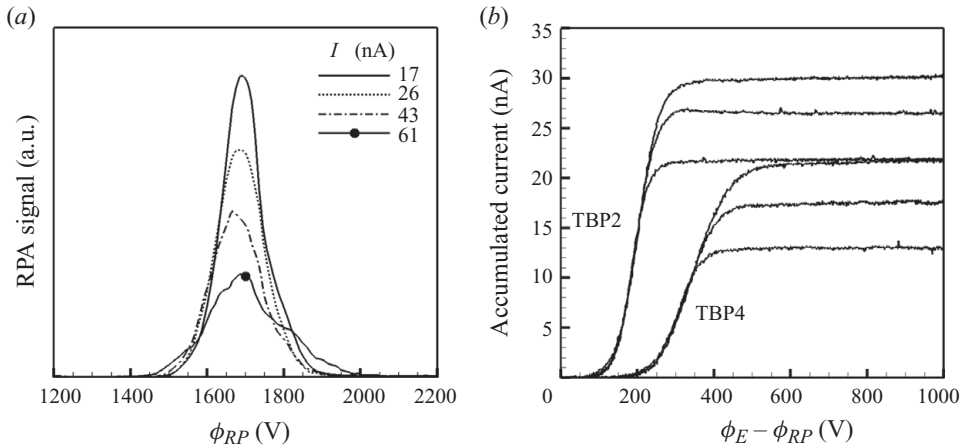
FIGURE 6. The voltage deficit of cone–jets does not depend on the flow rate. (*a*) Spectra for four PC3 flow rates measured at the beam axis with the electrostatic mirror. (*b*) Spectra for several TBP2 and TBP4 flow rates obtained with the cumulative retarding potential analyser.

the smaller its retarding potential. This is the trend observed in figure 5(*c*) for main droplets and the reason for the reduced stopping potentials of satellites in figure 4(*b*).

The natural variation of the charge-to-mass ratio is the most important, but not the only factor causing the broadness of the stopping potential distribution. For example, figure 5(*c*) shows that droplets with the same charge-to-mass ratio do have a narrow range of stopping potentials. In the absence of a correlation with the diameter and charge, this spread must be due to random processes in the breakup such as the variation of its axial location and the time-dependent Coulombic interaction between nearby droplets. These random contributions should average out, and (3.8) may then be used to approximate the average retarding potential of the droplets with a given charge-to-mass ratio ξ.

Going back to the problem of determining the value of the stopping potential ϕ_S to be inserted in (3.7), it is clear that the average stopping potential of droplets having the same charge-to-mass ratio as the jet is the correct answer. For the lowest flow rates producing main droplets only, the ξ-distribution resembles a narrow Gaussian centred at ξ_J, the stopping potential distributions are Gaussian-like and narrow as well, and therefore the average of the latter is approximately the average stopping potential of the droplets with a charge-to-mass ratio equal to that of the jet, $\langle\phi_{RP}\rangle \cong \langle\phi_{RP}(\xi = \xi_J)\rangle$. This greatly simplifies the determination of Δ, because it can be directly obtained from the peak of the retarding potential distribution. Conversely, when satellites are produced, the ξ-distribution of main droplets is not centred around ξ_J, this and the stopping potential distribution are much broader, and the peak of the stopping potential curve cannot be used to infer Δ. This complicates the estimation of Δ because it requires a detailed characterization of individual droplets.

3.3. *The total voltage deficit and flow rate are independent*

Figure 6(*a*) shows retarding potential distributions for several flow rates of PC3, measured at the beam axis with the electrostatic mirror. The potential of the emitter is 2040 V. At these low flow rates, no satellite droplets are generated, the resulting retarding potential and charge-to-mass-ratio distributions are narrow, and the emitter potential minus the average retarding potential is a good estimate of Δ.

The distributions have almost identical averages and widths despite a change in the flow rate by a factor of 7.1, and therefore Δ is constant, independent of the flow rate. This surprising fact is observed in every formamide, propylene carbonate and tributyl phosphate solution. For example, figure 6(b) shows distributions obtained with the cumulative retarding potential analyser for several flow rates of TBP2 and TBP4, all below the critical one triggering the formation of satellite drops. Unlike the data in figure 6(a) where only a small fraction of the beam is analysed, each one of these spectra captures the whole electrospray. It is striking that the distributions for a given solution are remarkably identical, regardless of the flow rate. The tail of the distributions does extend to higher potential deficits at increasing current, but this is an artefact of the increasing broadening of the beam (Gamero-Castaño 2008) and the underestimate of the stopping potential of droplets in the outer region of the beam. The electrostatic mirror is free from this problem, and it was shown in §3.2 that the minimum stopping potential of main droplets does not decrease with increasing flow rate, but remains constant. As mentioned before, we have observed this phenomenon in every liquid analysed with the electrostatic mirror, which includes all formamide and propylene carbonate solutions, and TBP3. The explanation of this interesting observation is now obvious: the physics of the cone–jet are such that the voltage deficit of the fluid in the jet does not depend on the flow rate and, according to the discussion in §3.2, the same is true for those main droplets with $\xi = \xi_J$. In the absence of satellites, all droplets have a charge-to-mass ratio similar to that of the jet, and therefore their retarding potential distributions are in a narrow voltage range that does not depend on the flow rate. When satellites are produced, the main droplets with higher charge-to-mass ratio are those formed by the shortest wavelengths unable to produce satellites, and therefore having $\xi \cong \xi_J$. Consequently, the retarding potentials of these drops, which are the lowest among the main droplet population for any given flow rate, must be in the same flow-rate-independent range observed in the absence of satellites. This is neatly illustrated by the distributions in figure 4(b) for $I = 40$ and $I = 149$ at 12°, the latter being the angular position of main droplets with lowest retarding potentials. In summary, Δ and Q are independent for all flow rates studied in this paper, regardless of whether satellite drops are produced or not.

Table 1 lists the total voltage deficit for each solution. The variable Δ augments with decreasing electrical conductivity and increasing dielectric constant. A deeper insight can be obtained with the help of dimensional analysis: upon using the scale $\phi_0 = \gamma^{2/3}/(K^{1/3}\varepsilon_0^{1/6}\rho^{1/6})$ and the experimental evidence to drop Q from the general dependence, the dimensionless total voltage deficit is given by

$$\frac{\Delta}{\phi_0} = \Pi_\Delta(Re, \varepsilon). \tag{3.9}$$

According to (3.6), Δ is proportional to the viscous voltage deficit, which is proportional to the viscosity. Therefore, Δ/ϕ_0 should be proportional to $1/Re$. This is confirmed in figure 7, which shows a linear dependence between the two variables:

$$\frac{\Delta}{\phi_0} = \alpha(\varepsilon) + \beta(\varepsilon)\frac{1}{Re}. \tag{3.10}$$

The slope and the y-intercept are functions of the dielectric constant. For a family of liquids with different conductivities but equal density, surface tension, viscosity and dielectric constant, Δ initially decreases linearly with $1/K$ and asymptotes to a constant value for large K. The dependence on the dielectric constant appears to
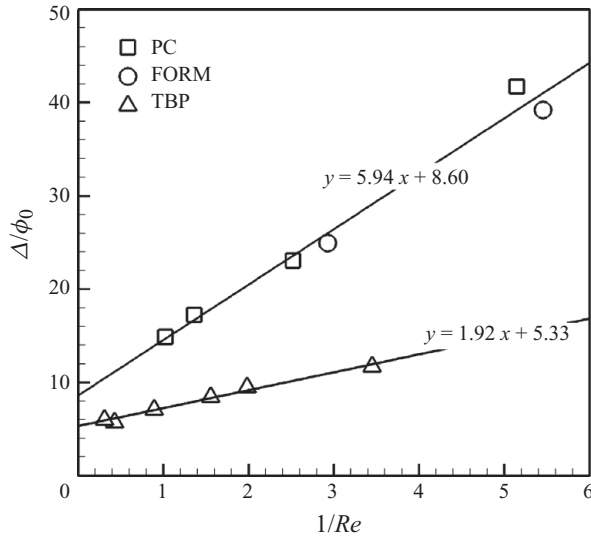
FIGURE 7. The dimensionless voltage deficit is a linear function of the inverse of the Reynolds number. The slope and y-intercept are functions of the dielectric constant.

be asymptotic at large ε, because the data for the very polar propylene carbonate and the extremely polar formamide fall near the same line. The linear fitting for the significantly less polar tributyl phosphate has smaller slope and y-intercept. The dependence of Δ/ϕ_0 on the Reynolds number suggests that a significant fraction of the electric power is degraded by viscous dissipation, while the y-intercept suggests that a fraction of the total voltage deficit is associated with ohmic dissipation and the generation of surface energy. The importance of viscous dissipation is puzzling in the context of existing cone–jet theories (Fernández de la Mora & Loscertales 1994; Gañán-Calvo 2004), because these models predict currents and jet diameters that do not depend on the viscosity.

We next estimate the surface voltage deficit to determine its relative importance. The parameter Δ_γ, given by (3.7), may be evaluated with the values of the electrospray current, flow rate and average diameter of main droplets. The factor 1.89 associated with inviscid jet breakup is a good estimate for the ratio between the average droplet and jet diameters. Figure 8(a) displays Δ_γ/Δ as a function of Δ_γ/ϕ_0. The surface voltage deficit is between 10 and 22 % of the total voltage deficit, and therefore the largest fraction of Δ must be associated with dissipative effects. This result is important because the degradation of energy is concentrated in the transition region, and therefore the total voltage deficit is directly related to the physics of this area. The dependence of the surface voltage deficit on the operational parameters can be determined by substituting into (3.7) the expression for the electrospray current, $I = a(\varepsilon)(\gamma Q K)^{1/2}$, and Gañán-Calvo's diameter scale, $r_{GC} = (\rho \varepsilon_0 Q^3/\gamma K)^{1/6}$:

$$\frac{\Delta_\gamma}{\phi_0} = g(\varepsilon). \tag{3.11}$$

These laws for the current and jet diameter, which are known to fit the experimental data well, show that the dimensionless surface voltage deficit is a function of only the dielectric constant, and therefore a fraction of the y-intercept, $\alpha(\varepsilon)$. Several values for propylene carbonate depart from (3.11). This is likely to be due to our indirect
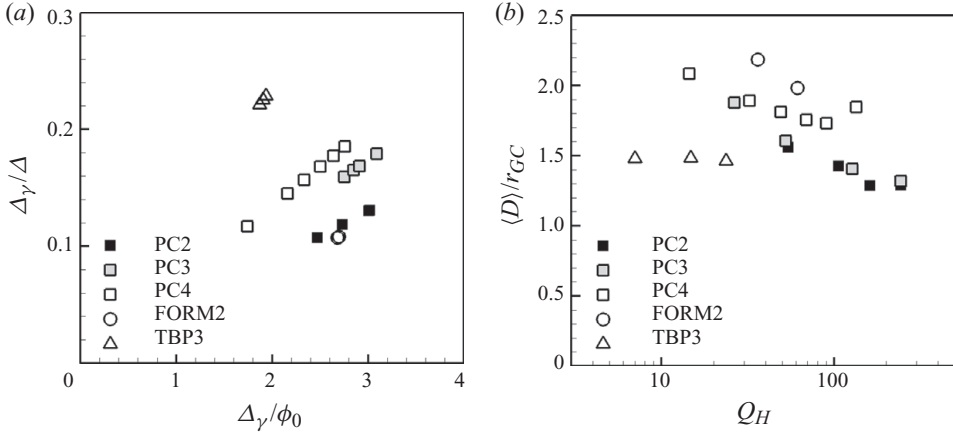
FIGURE 8. (*a*) Ratio between the surface and total voltage deficits plotted against the dimensionless surface voltage deficit. The surface voltage deficit is a small fraction of the total voltage deficit, and therefore the ohmic and viscous dissipations are the dominant contributions. (*b*) Average diameter of electrospray droplets in r_{GC} units versus dimensionless flow rate.

estimate of the jet diameter, which is computed from an incomplete sample of the droplet population. Figure 8(*b*) shows the average diameters used for the estimate, obtained from samples at or near the beam axis. The droplet diameters normalized with the r_{GC} scale should display a horizontal trend, but they depend on the flow rate for the case of propylene carbonate. In our opinion, this is a deficiency of the measurements, rather than of the r_{GC} scaling: the average diameter cannot be computed accurately from a droplet sample limited to the beam axis, and it does not account for the angular segregation of droplets by diameters and charge-to-mass ratios. The more direct estimate of the jet diameter by Gamero-Castaño & Hruby (2002) strongly supports Gañán-Calvo's diameter scaling, and therefore the validity of (3.11). In the next section, we will show that r_{GC}, multiplied by $\varepsilon^{1/6}$, is indeed the correct characteristic radial and axial length of the transition region.

3.4. *The geometric scaling of the transition region*

The dissipative processes are concentrated in the cone-to-jet transition because this is where the largest velocity gradients and electric fields are. Therefore, the scaling law (3.10) for the total voltage deficit must convey information on the physics of the transition region. To extract this information, we will integrate the ohmic and viscous power densities over the cone–jet volume, and find approximate expressions for P_Ω and P_μ in terms of the radial r_n and axial l_n characteristic lengths of the transition region. These will then be inserted in (3.10) to find the forms of r_n and l_n. The viscous dissipation power density in the axisymmetric cone–jet is given by

$$\boldsymbol{\tau}_\mu : \nabla \boldsymbol{v} = 2\mu \left[\left(\frac{\partial v_r}{\partial r} \right)^2 + \left(\frac{v_r}{r} \right)^2 + \left(\frac{\partial v_z}{\partial z} \right)^2 + \frac{1}{2} \left(\frac{\partial v_z}{\partial r} + \frac{\partial v v_r}{\partial z} \right)^2 \right]. \qquad (3.12)$$

It can be shown that the term in the last bracket is negligible, and the equation of continuity may then be used to bound $\boldsymbol{\tau}_\mu : \nabla \boldsymbol{v}$:

$$2\mu \left(\frac{\partial v_z}{\partial z} \right)^2 < \boldsymbol{\tau}_\mu : \nabla \boldsymbol{v} < 4\mu \left(\frac{\partial v_z}{\partial z} \right)^2. \qquad (3.13)$$

We now assume a flat velocity profile, $v_z = Q/\pi R^2(z)$, and integrate the upper bound over the volume of the cone–jet to obtain

$$P_\mu \approx \int_{-\infty}^{\infty} \frac{8\mu Q^2}{\pi R^4} \left(\frac{dR}{dz}\right)^2 dz \approx \frac{16\mu Q^2}{3\pi r_n^3}\left(1+\frac{r_n}{l_n}\right), \quad \Delta_\mu \approx \frac{16\mu Q^{3/2}}{3\pi a\gamma^{1/2}K^{1/2}}\frac{1}{r_n^3}\left(1+\frac{r_n}{l_n}\right). \tag{3.14}$$

The value of dR/dz is $\tan(49.2°) \cong 1$ in the Taylor cone, of the order of r_n/l_n in the transition region and negligible in the jet. We also use the scaling law $I = a(\varepsilon)(\gamma K Q)^{1/2}$ to express Δ_μ. It is worth noting that the viscous dissipation is proportional to the viscosity and strongly depends on r_n.

The net ohmic power is given in (3.2) and can be estimated as

$$P_\Omega \approx \int_{-\infty}^{\infty} \frac{I_c^2}{K\pi R^2}\, dz \approx \frac{I^2}{K\pi r_n}\left(1+\frac{l_n}{4r_n}\right), \quad \Delta_\Omega \approx \frac{a\gamma^{1/2}Q^{1/2}}{\pi K^{1/2}r_n}\left(1+\frac{l_n}{4r_n}\right), \tag{3.15}$$

where I_c stands for the intensity of the conduction current in the liquid bulk. The viscous, ohmic and surface voltage deficits may now be inserted in (3.10) to find the scalings of r_n and l_n:

$$\frac{8\mu Q^{3/2}\varepsilon_0^{1/6}\rho^{1/6}}{3\pi a\gamma^{7/6}K^{1/6}}\frac{1}{r_n^3}\left(1+\frac{r_n}{l_n}\right) + \frac{aQ^{1/2}\varepsilon_0^{1/6}\rho^{1/6}}{\pi K^{1/6}\gamma^{1/6}}\frac{1}{r_n}\left(1+\frac{l_n}{4r_n}\right)$$
$$= \alpha(\varepsilon) - g(\varepsilon) + \beta(\varepsilon)\frac{\mu K^{1/3}}{\rho^{1/3}\varepsilon_0^{1/3}\gamma^{2/3}}. \tag{3.16}$$

The viscous voltage deficit is clearly responsible for the proportionality between the total voltage deficit and the inverse of the Reynolds number, while the dimensionless ohmic voltage deficit is a fraction of the y-ordinate $\alpha(\varepsilon)$. More importantly, (3.16) requires that both r_n and l_n have the same scaling r_t:

$$r_n = N(\varepsilon)r_t, \quad l_n = M(\varepsilon)r_t, \quad r_t = \left(\frac{\rho\varepsilon\varepsilon_0 Q^3}{\gamma K}\right)^{1/6}. \tag{3.17}$$

The characteristic radial and axial lengths of the transition region are proportional to r_t, the proportionality constants being functions of ε. Interestingly, this unique scale can be expressed as the geometric average, $r_t = \sqrt{r_{\rho\gamma}r_{FM}}$, of two lengths associated with important balances in the cone–jet: $r_{FM} = (\varepsilon\varepsilon_0 Q/K)^{1/3}$ is the electrical relaxation length or distance from the Taylor cone's vertex where the electrical relaxation time and the fluid's residence time become comparable, causing the breakdown of Taylor's solution (Fernández de la Mora & Loscertales 1994); $r_{\rho\gamma}$ is the radius of the cone at which the dynamic pressure equals the capillary pressure, $r_{\rho\gamma} = (\rho Q^2/\gamma)^{1/3}$. It is worth noting that r_t is identical to r_{GC} except for the presence of the small factor $\varepsilon^{1/6}$, and therefore our inclusion of the dielectric constant may seem arbitrary. However, there are three key points that justify this: first, in our view, r_t is the geometric mean of two physical lengths, and although the group $(\varepsilon_0 Q/K)^{1/3}$ has dimensions of length, it does not have any physical significance unless the dielectric constant is included. Second, electrical relaxation phenomena are clearly important in the transition region, as demonstrated by the dependence of both the electrospray current and the total voltage deficit on the dielectric constant. Third, the characteristic axial length L resulting from the theory yielding r_{GC} is much larger than r_{GC} and has a different
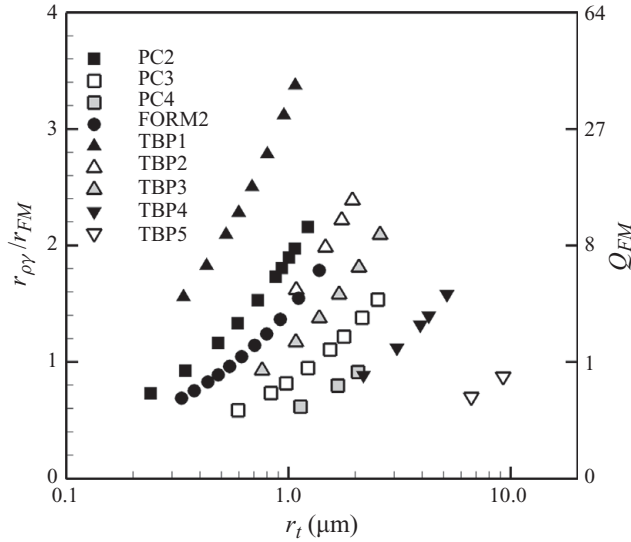
FIGURE 9. The electrical relaxation length r_{FM} and the distance $r_{\rho\gamma}$ from the cone apex where the dynamic pressure equals the capillary pressure are comparable for all cone–jets in this study. The geometric average of $r_{\rho\gamma}$ and r_{FM}, r_t, is the characteristic length of the transition region.

form, $L = (\rho^2 K Q^3/\gamma^2\varepsilon_0)^{1/3}$ (Gañán-Calvo 2004); furthermore, the combination of r_{GC} and L produces a total voltage deficit that depends on the flow rate. Therefore, Gañán-Calvo's theory and its characteristic lengths r_{GC} and L are not applicable to our cone–jets.

The merging of $r_{\rho\gamma}$ and r_{FM} into a single characteristic length suggests that $r_{\rho\gamma}$ and r_{FM} need to be comparable for any combination of the flow rate, density, surface tension, viscosity and dielectric constant associated with a stable cone–jet. This is confirmed in figure 9, which displays r_t, the ratio $r_{\rho\gamma}/r_{FM}$ and Q_{FM} for the electrosprays studied in this paper: $r_{\rho\gamma}$ is typically larger than r_{FM}, but their ratio is restricted to a range between 0.5 and 3.5. The significance of the ratio $r_{\rho\gamma}/r_{FM}$ was first noticed by Fernández de la Mora & Loscertales (1994), who cast it in the form of the dimensionless flow rate $Q_{FM} = (r_{\rho\gamma}/r_{FM})^3$, and pointed out that this group was of order one for a wide range of liquids, flow rates and electrical conductivities. $N(\varepsilon)$ and $M(\varepsilon)$ can be estimated by solving the algebraic equations

$$\frac{16(M+N)}{3a\pi M N^3 \beta \varepsilon^{1/2}} = 1, \quad \frac{a(M+4N)}{4\pi N^2(\alpha - g)\beta \varepsilon^{1/6}} = 1. \tag{3.18}$$

The resulting values of N and M for formamide, propylene carbonate and tributyl phosphate are 0.26 and 6.33, 0.28 and 5.28, and 0.52 and 5.12, respectively. Thus, the transition region becomes more slender for increasing dielectric constant, which is in agreement with the numerical results of Higuera (2003). Physically, this is due to the shielding of the electric field inside the liquid by the polarization charge, which slows down the injection of charge from the liquid bulk into the surface in the attempt to restore equipotentiality. We expect to have underestimated the values of M and N by factors of order one, due to the strong dependence of $\tau_\mu : \nabla v$ on $R(z)$, and the disproportionate weight of the exit radius of the transition region in the evaluation of Δ_μ. Thus, when solving (3.18), the resulting N is more representative of $R(z)$ near the end of the transition region, than of the averaged or characteristic radius r_n. The
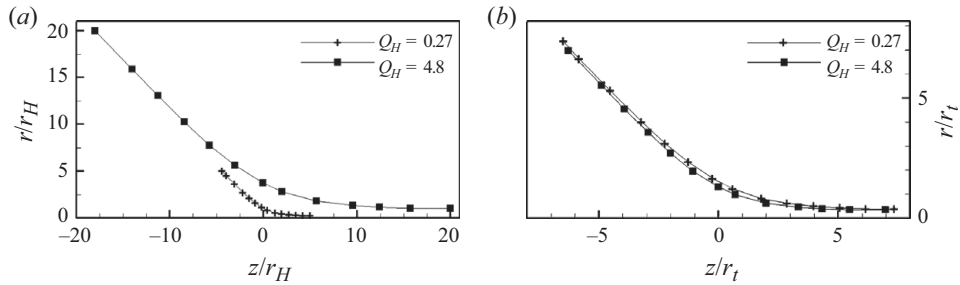
FIGURE 10. (*a*) Profiles of the transition region computed by Higuera (2003) for a liquid with a dielectric constant of 5 and a Reynolds number of 1, and for two dimensionless flow rates $Q_H = 0.27$ and 4.8. (*b*) The two profiles coincide when they are plotted in units of the characteristic length r_t.

underestimate of r_n also translates into an underestimate of l_n, since a smaller axial length will be required to produce the ohmic voltage deficit.

Since the radial and longitudinal characteristic lengths have the same scaling, the geometry of the transition region normalized with r_t should be insensitive to changes of the liquid flow rate, surface tension, density and viscosity. An independent validation of this observation can be attempted with actual geometries of cone–jets, e.g. using the numerical solutions reported by Higuera (2003). Figure 2 of this reference shows profiles of the transition region for a liquid with a dielectric constant of 5 and a Reynolds number of 1, and for two different flow rates, $Q_H = 0.27$ and $Q_H = 4.8$. Figure 10(*a*) reproduces these profiles using the same length unit as in the original article, $r_H = (\varepsilon_0^2 \gamma / \rho K^2)^{1/3}$, which is the same for both flow rates. The 17.7-fold change in Q_H results in an obvious variation of the transition region's size. However, when the radial and axial coordinates are rescaled with r_t,

$$\frac{x}{r_t} = \frac{1}{\varepsilon^{1/6} Q_H^{1/2}} \frac{x}{r_H}, \tag{3.19}$$

the resulting profiles are nearly identical, as shown in figure 10(*b*). Although not attempted, we could have obtained a better agreement by slightly shifting the origin of the axial coordinates, which is fixed in Higuera's model by an asymptotic relation within an error of $r_t / \varepsilon^{1/6} Q_H^{1/2}$ (approximately within 1.4 units in figure 10*b*). The merging of the very different profiles of figure 10(*a*) when using r_t as length unit is a striking result. In our opinion, it is a sign of the accuracy of Higuera's model and the correctness of r_t as the fundamental scale of the transition region. Furthermore, defining the centre of the transition region as the axial location where the conduction and convected currents become equal, and the characteristic radius r_n as the radius of the cone–jet at this point, figure 3(*a*) of Higuera yields the centre at $z/r_t \cong 1.8$, and a characteristic radius $r_n/r_t \cong 0.67$. This value for $\varepsilon = 5$ compares well with our experimental estimate of $r_n/r_t \cong 0.52$ for tributyl phosphate, $\varepsilon = 8.91$. Furthermore, defining the characteristic length of the transition region as the length within which 80 % of the conduction current becomes convected current, Higuera's figure yields a value of $l_n/r_t \cong 9.2$, while our estimate for tributyl phosphate is $l_n/r_t \cong 5.12$. The likely reason for our underestimate of the characteristic lengths has been outlined above.

We have derived the scale r_t using an experimental observation (the independence between the droplets' voltage deficit and the flow rate) combined with a macroscopic balance of the mechanical energy in the cone–jet, and it is worth exploring whether

this result may shed some light on the balance of forces in the transition region. To this end, we start with the momentum equation in the axial direction given by Gañán-Calvo (2004) for a slender jet,

$$\frac{d}{dz}\left(\frac{1}{2\pi^2}\frac{\rho Q^2}{R^4}\right) + \frac{d}{dz}\left(\frac{\gamma}{R}\right) + \frac{6\mu Q}{\pi R^2}\frac{d}{dz}\left(\frac{1}{R}\frac{dR}{dz}\right) = \frac{2\sigma E_s}{R} + \frac{\varepsilon_0}{2}\frac{d}{dz}\left[(\varepsilon - 1)E_s^2 + E_n^{o^2}\right],$$

(3.20)

which is approximately valid in the transition region and includes conservation of mass and the balance of stresses in the surface of revolution. The pressure is separated into capillary, polarization and electrostatic components, while the viscous shear is substituted by the electric drag $2\sigma E_s/R$ on the surface. The identical scaling of the radial and axial lengths suggests that the solution of this equation when properly normalized, $R(z/r_t)/r_t$, must be independent of the flow rate. In order to non-dimensionalize (3.20) in a manner consistent with the sought solution, we express the surface charge and the tangential component of the electric field in terms of the surface and conduction currents, $\sigma = I_s R/2Q$ and $E_s = I_c/\pi R^2 K$, and use r_t and $(\gamma Q K)^{1/2}$ as the length and current scales to write

$$\frac{Q_{FM}^{1/2}}{2\pi}\frac{d}{d\tilde{z}}\left(\frac{1}{\tilde{R}^4}\right) + \pi\frac{d}{d\tilde{z}}\left(\frac{1}{\tilde{R}}\right) + \frac{6}{\varepsilon^{1/3}Re}\frac{1}{\tilde{R}^2}\frac{d}{d\tilde{z}}\left(\frac{1}{\tilde{R}}\frac{d\tilde{R}}{d\tilde{z}}\right)$$
$$= \frac{\tilde{I}_s\tilde{I}_c}{\tilde{R}^2} + \frac{d}{d\tilde{z}}\left[\frac{(\varepsilon - 1)}{2\pi\varepsilon Q_{FM}^{1/2}}\frac{\tilde{I}_c^2}{\tilde{R}^4} + \frac{\pi\varepsilon Q_{FM}^{1/2}}{8}\tilde{I}_s^2\tilde{R}^2\right], \quad (3.21)$$

where symbols capped with a tilde stand for dimensionless variables. Since the electric drag $\tilde{I}_s\tilde{I}_c/\tilde{R}^2$ is the driving force, the independence of $\tilde{R}(\tilde{z})$ of the flow rate suggests that any term multiplied by a power of Q_{FM} is negligible. Thus, the dominant balance in the transition region for most cone–jets appears to be between the capillary and the electric drag terms, while the viscous stress may replace the capillary pressure at small Reynolds numbers (i.e. in fluids with high viscosities and/or high electrical conductivities). Interestingly, the r_t and $I \sim (\gamma Q K)^{1/2}$ scaling also make the asymptotic boundary conditions for the momentum equation and the electric field (Higuera 2003) nearly independent of the flow rate: the asymptotic value of the electric field far upstream in the Taylor cone is $E \sim I/(K R^2)$, which is independent of the flow rate, while the asymptotic value of the jet radius far downstream, $R \sim (\varepsilon_0\rho^2/\gamma)^{1/8} Q^{3/4}/(I^{1/4}z^{1/8})$, has a negligible dependence on the flow rate, $\tilde{R} \sim Q_{FM}^{1/16}/(\tilde{I}^{1/4}\tilde{z}^{1/8}\varepsilon^{1/8})$. In other words, both the equation of conservation of momentum and the required far-field boundary conditions, when made dimensionless with r_t and $(\gamma Q K)^{1/2}$, are compatible with a solution $\tilde{R}(\tilde{z})$ that does not depend on the flow rate.

Finally, the dissipation of energy that predominantly takes place in the transition region increases the temperature of the fluid by the amount ΔT:

$$\Delta T = \frac{P_\Omega + P_\mu}{\rho Q c} \sim \frac{a(\varepsilon)\beta(\varepsilon)}{c}\left(\frac{\mu^2\gamma K}{\varepsilon_0 Q\rho^3}\right)^{1/2}, \quad (3.22)$$

where the asymptotic relation is valid for small Reynolds numbers. (The smaller the Re, the larger the viscous dissipation and the temperature increase.) The magnitude of ΔT is substantial for cone–jets with high electrical conductivities and low flow rates. For example, although the temperature increase is just $1\,°C$ for PC4 at $I = 18$ nA, we estimate values as high as 11 and $27\,°C$ for PC2 and FORM1 near the

minimum flow rates. One of the most interesting research areas in electrosprays is the study of nanojets and the associated phenomenology such as the emission of nanodroplets and molecular ions. The formation of these nanometric structures requires the electrospraying of fluids with high electrical conductivities, typically of the order of $0.5\,\mathrm{S\,m^{-1}}$ and higher, and is favoured by operation at low flow rates. It is evident that temperature variations in these cone–jets are quite large and will need to be accounted for in their modelling.

4. Conclusions

We have studied electrosprays in the cone–jet mode in a wide range of flow rates, electrical conductivities and employing three fluids with significantly different dielectric constants. Although the main experimental thrust has been the characterization of the voltage deficit via retarding potential spectrometry, we have also measured other parameters such as the total current and the charge and diameter of droplets. Our interest in the voltage deficit, which is a droplet parameter, stems from its relationship with the physics of the transition region of the cone–jet. In fact, we find that the largest fraction of the voltage deficit results from the viscous and ohmic dissipations of energy taking place in this area. The retarding-potential measurements show that the voltage deficit strongly depends on the electrical conductivity, viscosity and dielectric constant of the fluid, and is independent of the flow rate. This last result has profound implications in the physics of cone–jets: combined with the well-established law for the current, $I \sim (\gamma Q K)^{1/2}$, it requires that both the radial and axial lengths of the transition region scale with a single characteristic length, $r_t = (\rho \varepsilon \varepsilon_0 Q^3 / \gamma K)^{1/6}$, where r_t is the geometric mean of an electrical relaxation length and a length resulting from the balance of capillary and dynamic pressures. The fact that the values of these last two lengths are similar throughout a wide range of operational conditions, together with the substantial dependence of the electrospray current and the voltage deficit on the dielectric constant, indicate that electrical relaxation effects are important in the transition region.

We have further confirmed the validity of r_t by showing that Higuera's numerical solution for the profile of the transition region, non-dimensionalized with r_t, is invariant to changes of the flow rate. Higuera's model solves the full electrohydrodynamic equations for the cone–jet with appropriate far-field boundary conditions. Finally, we notice that the dissipation of energy significantly increases the temperature of fluids with moderate and high electrical conductivities. The temperature field, and the resulting influence on the transport coefficients and surface energy, will need to be considered when modelling the physics of cone–jets in this most interesting high-conductivity regime.

Supplementary material is available at journals.cambridge.org/flm

REFERENCES

ASHGRIZ, N. & MASHAYEK, F. 1995. Temporal analysis of capillary jet breakup. *J. Fluid Mech.* **291**, 163–190.

CLOUPEAU, M. & PRUNET-FOCH, B. 1989 Electrostatic spraying of liquids in cone–jet mode. *J. Electrostat.* **22**, 135–159.

CLOUPEAU, M. & PRUNET-FOCH, B. 1990 Electrostatic spraying of liquids. Main functioning modes. *J. Electrostat.* **25**, 165–184.

COLLINS, R. T., HARRIS, M. T. & BASARAN, O. A. 2007 Breakup of electrified jets. *J. Fluid Mech.* **588**, 75–129.

COLLINS, R. T., JONES, J. J., HARRIS, M. T. & BASARAN, O. A. 2008 Electrohydrodynamic tip streaming and emission of charged drops from liquid cones. *Nat. Phys.* **4**, 149–154.

COOK, K. D. 1986 Electrohydrodynamic mass-spectrometry. *Mass Spectrom. Rev.* **5**, 467–519.

FENN, J. B., MANN, M., MENG, C. K., WONG, S. K. & WHITEHOUSE, C. M. 1989 Electrospray ionization for mass spectrometry of large biomolecules. *Science* **246**, 64–71.

FERNÁNDEZ DE LA MORA, J. 2007 The fluid dynamics of Taylor cones. *Annu. Rev. Fluid Mech.* **39**, 217–243.

FERNÁNDEZ DE LA MORA, J. & LOSCERTALES, I. G. 1994 The current transmitted through an electrified conical meniscus. *J. Fluid Mech.* **260**, 155–184.

GAMERO-CASTAÑO, M. 2008 The structure of electrospray beams in vacuum. *J. Fluid Mech.* **604**, 339–368.

GAMERO-CASTAÑO, M. 2009 Retarding potential and induction charge detectors in tandem for measuring the charge and mass of nanodroplets. *Rev. Sci. Instrum.* **80**, 053301.

GAMERO-CASTAÑO, M., AGUIRRE-DE-CARCER, I., DE JUAN, L. & FERNÁNDEZ DE LA MORA, J. 1998 On the current emitted by Taylor cone jets of electrolytes in vacuo: implications for liquid metal ion sources. *J. Appl. Phys.* **83**, 2428–2434.

GAMERO-CASTAÑO, M. & HRUBY, V. 2001 Electrospray as a source of nanoparticles for efficient colloid thrusters. *J. Propul. Power* **17**, 977–987.

GAMERO-CASTAÑO, M. & HRUBY, V. 2002. Electric measurements of charged sprays emitted by cone–jets. *J. Fluid Mech.* **459**, 245–276.

GAMERO-CASTAÑO, M. & MAHADEVAN, M. 2009 Sputtering yields of Si, SiC and B_4C under nanodroplet bombardment at normal incidence. *J. Appl. Phys.* **106**, 054305.

GAÑÁN-CALVO, A. M. 1997 Cone–jet analytical extension of Taylor's electrostatic solution and the asymptotic universal scaling laws in electrospraying. *Phys. Rev. Lett.* **79**, 217–220.

GAÑÁN-CALVO, A. M. 2004 On the general scaling theory for electrospraying. *J. Fluid Mech.* **507**, 203–212.

GAÑÁN-CALVO, A. M., DÁVILA, J. & BARRERO, A. 1996 Current and droplet size in the electrospraying of liquids. Scaling laws. *J. Aerosol Sci.* **28**, 249–275.

HIGUERA, F. J. 2003 Flow rate and electric current emitted by a Taylor cone. *J. Fluid Mech.* **484**, 303–327.

HUBERMAN, M. N. 1970 Measurement of the energy dissipated in the electrostatic spraying process. *J. Appl. Phys.* **41**, 578–584.

KYRITSIS, D. C., ROYCHOUDHURY, S., MCENALLY, C. S., PFEFFERLE, L. D. & GOMEZ, A. 2004 Mesoscale combustion: a first step towards liquid fueled batteries. *Exp. Therm. Fluid Sci.* **28**, 763–770.

LÓPEZ-HERRERA, J. M. & GAÑÁN-CALVO, A. M. 2004 A note on charged capillary jet breakup of conducting liquids: experimental validation of a viscous one-dimensional model. *J. Fluid Mech.* **501**, 303–326.

LOSCERTALES, I. G., BARRERO, A., GUERRERO, I., CORTIJO, R., MARQUEZ, M. & GAÑÁN-CALVO, A. M. 2002 Micro/nano encapsulation via electrified coaxial liquid jets. *Science* **295**, 1695–1698.

MCEWEN, A. B., NGO, H. L., LECOMPTE, K. & GOLDMAN, J. L. 1999 Electrochemical properties of imidazolium salt electrolytes for electrochemical capacitor applications. *J. Electrochem. Soc.* **146**, 1687–1695.

PREWETT, P. D. & MAIR, G. L. R. 1991 *Focused Ion Beams from Liquid Metal Ion Sources*, Ch. IV. Research Studies Press.

RIDDICK, J. A., BUNGER, W. B. & SAKANO, T. K. 1986 *Organic Solvents. Physical Properties and Methods of Purification*, 4th edn. Wiley.

ROSELL-LLOMPART, J. & FERNÁNDEZ DE LA MORA, J. 1994 Generation of monodisperse droplets 0.3 to 4 mm in diameter from electrified cone–jets of highly conducting and viscous liquids. *J. Aerosol Sci.* **25**, 1093–1119.

TAYLOR, G. I. 1964 Disintegration of water drops in an electric field. *Proc. R. Soc. Lond.* A **280**, 383–397.

ZELENY, J. 1914 The electrical discharge from liquid points, and a hydrostatic method of measuring the electrical intensity at their surfaces. *Phys. Rev.* **3**, 69–91.

Supporting Online Material

Appendix to "Energy Dissipation in Electrosprays and the Geometric Scaling of the Transition Region of Cone-Jets"

By Manuel Gamero-Castano

This material has not been copy-edited or typeset by Cambridge University

Press: its format is entirely the responsibility of the author

Macroscopic equations of mechanical energy and internal energy for an electrified jet.

The equations of conservation of mass and charge, the Navier-Stokes equations, and the Laplace equation for the electrical potential completely describe the hydrodynamics and geometry of the cone-jet (Melcher & Taylor 1969, Saville 1997, Higuera 2003). The steady-state momentum equation and the resulting equation of mechanical energy for an incompressible fluid can be written as

$$\rho\,\mathbf{v}\cdot\nabla\mathbf{v} = -\nabla p + \nabla\cdot\boldsymbol{\tau}_\mu + \nabla\cdot\boldsymbol{\tau}_M \qquad (A.1)$$

$$\rho\nabla\cdot(\mathbf{v}\,\mathbf{v}^2/2) = -\nabla\cdot(p\mathbf{v}) + \nabla\cdot(\boldsymbol{\tau}_\mu\cdot\mathbf{v}) - \boldsymbol{\tau}_\mu{:}\nabla\mathbf{v} + \mathbf{v}\cdot\nabla\cdot\boldsymbol{\tau}_M \qquad (A.2)$$

The electrical forces acting on the fluid are modeled with the Maxwell stress tensor $\boldsymbol{\tau}_M$

$$\boldsymbol{\tau}_M = \varepsilon\varepsilon_0\mathbf{E}\mathbf{E} - \frac{1}{2}\varepsilon\varepsilon_0\left[1 - \frac{\rho}{\varepsilon}\left(\frac{\partial\varepsilon}{\partial\rho}\right)_T\right]\mathbf{E}\cdot\mathbf{E}\boldsymbol{\delta} \qquad (A.3)$$

which yields the volumetric force

$$\nabla\cdot\boldsymbol{\tau}_M = \frac{1}{2}\varepsilon_0\nabla\left[\rho\left(\frac{\partial\varepsilon}{\partial\rho}\right)_T E^2\right] - \frac{1}{2}\varepsilon_0 E^2\nabla\varepsilon + \rho^e\mathbf{E} \qquad (A.4)$$

This force and the associated terms in the momentum and mechanical energy equations are usually ignored, because to a high degree of accuracy the electrostriction force in the

A.1

incompressible fluid and the charge density ρ^e can be regarded as negligible, and the dielectric constant can be treated as uniform throughout the fluid. Thus the coupling between electrostatic forces and hydrodynamics is a surface effect, and is enforced by requiring that the free surface of the cone-jet is in mechanical equilibrium. The balance of stresses in the interface Σ_0 (see figure 4(b)) can be written as

$$(\gamma\boldsymbol{\delta}\nabla\cdot\mathbf{n} - p\boldsymbol{\delta} + \boldsymbol{\tau}_\mu + \boldsymbol{\tau}_M^i)\cdot\mathbf{n} = \boldsymbol{\tau}_M^o\cdot\mathbf{n} \tag{A.5}$$

where $\mathbf{n}$ is the outward normal vector and the superscripts i and o denote the liquid bulk and the surrounding vacuum respectively. In particular, the tangential component of (A.5) in the rz plane is

$$\mathbf{t}\cdot\boldsymbol{\tau}_\mu\cdot\mathbf{n} = \mathbf{t}\cdot(\boldsymbol{\tau}_M^o - \boldsymbol{\tau}_M^i)\cdot\mathbf{n} = \varepsilon_0 E_z (E_r^o - \varepsilon E_r^i) = \sigma E_z \tag{A.6}$$

$$\mathbf{t}\cdot\boldsymbol{\tau}_\mu\cdot\mathbf{n} = 2\mu\frac{\partial \mathbf{v}_z}{\partial r}\bigg|_{\Sigma_0} \tag{A.7}$$

where σ stands for the surface charge density in the interface.

The macroscopic balance of the mechanical energy in the cone-jet is obtained by integrating (A.2) over the volume Π bounded by the surfaces Σ_0, Σ_1, and Σ_2 (see figure 4(b)). The integration of every term with the exception of $\nabla\cdot(\boldsymbol{\tau}_\mu\cdot\mathbf{v})$ is trivial:

$$\int_\Pi \rho\nabla\cdot(\mathbf{v}\frac{\mathbf{v}^2}{2})dV = \int_{\Sigma_0,\Sigma_1,\Sigma_2} \rho\frac{\mathbf{v}^2}{2}\mathbf{v}\cdot d\mathbf{A} = 0 - \rho Q\frac{\mathbf{v}_1^2}{2} + \rho Q\frac{\mathbf{v}_2^2}{2} \tag{A.8}$$

$$\int_\Pi \nabla\cdot(p\mathbf{v})dV = \int_{\Sigma_0,\Sigma_1,\Sigma_2} p\mathbf{v}\cdot d\mathbf{A} = 0 - Q\,p_1 + Q\,p_2 \tag{A.9}$$

$$\int_\Pi \boldsymbol{\tau}_\mu{:}\nabla\mathbf{v}\,dV = P_\mu \tag{A.10}$$

P_μ is the net viscous power dissipated in the cone-jet. To integrate $\nabla\cdot(\boldsymbol{\tau}_\mu\cdot\mathbf{v})$ we make use of the balance of stresses in Σ_0, equation (A.6):

A.2

$$\int_{\Pi} \nabla \cdot (\boldsymbol{\tau}_{\mu} \cdot \mathbf{v}) \, dV = \int_{\Sigma_0, \Sigma_1, \Sigma_2} (\boldsymbol{\tau}_{\mu} \cdot \mathbf{v}) \cdot d\mathbf{A} = \int_{\Sigma_0} \sigma E_z \mathbf{v} dA - 2\mu Q \frac{\partial \mathbf{v}_z}{\partial z} \bigg|_{\Sigma_1} + 2\mu Q \frac{\partial \mathbf{v}_z}{\partial z} \bigg|_{\Sigma_2} \quad \text{(A.11)}$$

where we have assumed flat velocity profiles at Σ_1 and Σ_2. The last two terms in (A.11) are negligible because the viscous stresses rapidly decay both upstream and downstream of the transition region. To advance further we write the differential of area as $dA = 2\pi R ds$ (s is the arc length of the generatrix g_0 measured from the intersection with Σ_1)

$$\int_{g_0} 2\pi R \mathbf{v} \sigma (E_z ds) = \int_{g_0} I_s (-d\phi) \quad \text{(A.12)}$$

and notice that charge conservation requires the sum of the surface and bulk conduction currents crossing any $r\theta$ plane to be constant, and equal to the total electrospray current I

$$\int_{g_0} I_s (-d\phi) = -\int_{g_0} (I - I_c) d\phi = I(\phi_1 - \phi_2) + \int_{g_0} I_c d\phi \quad \text{(A.13)}$$

We now integrate the last term by parts to obtain

$$\int_{g_0} I_c d\phi = \int_{g_0} d(I_c \phi) - \int_{g_0} \phi \, dI_c = I_c \phi \big|_{\Sigma_2} - I_c \phi \big|_{\Sigma_1} + \int_{\Sigma_0} \phi K \mathbf{E}^i \cdot d\mathbf{A} \quad \text{(A.14)}$$

In this step we have used the equation of conservation of charge in differential form, which requires the variation of the conduction current to be balanced by the charge injected onto the surface, $dI_c = -K\mathbf{E}^i \cdot d\mathbf{A}\big|_{\Sigma_0}$. Note that I_c asymptotes to the total current I upstream in the Taylor cone, and is negligible downstream of the transition region. We now use the Gauss theorem to evaluate the last integral in (A.14)

$$\int_{\Sigma_0} \phi K \mathbf{E}^i \cdot d\mathbf{A} = \int_{\Pi} \nabla \cdot (\phi K \mathbf{E}) \, dV - \int_{\Sigma_1, \Sigma_2} \phi K \mathbf{E}^i \cdot d\mathbf{A} = -\int_{\Pi} \mathbf{J} \cdot \mathbf{E} \, dV + I_c \phi \big|_{\Sigma_1} - I_c \phi \big|_{\Sigma_2 \, 1} \quad \text{(A.15)}$$

$$\int_{\Pi} \nabla \cdot (\phi K \mathbf{E}) \, dV = \int_{\Pi} K\phi \nabla \cdot \mathbf{E} \, dV + \int_{\Pi} K \mathbf{E} \nabla \phi \, dV = 0 - \int_{\Pi} \mathbf{J} \cdot \mathbf{E} \, dV$$

$$\int_{\Sigma_1, \Sigma_2} \phi K \mathbf{E}^i \cdot d\mathbf{A} = -I_c \phi \big|_{\Sigma_1} + I_c \phi \big|_{\Sigma_2}$$

The last integral in (A.15) is the net ohmic dissipation in the cone-jet, P_Ω. Thus, the sought integral of $\nabla \cdot (\boldsymbol{\tau}_\mu \cdot \mathbf{v})$ over the volume of the cone-jet can be written as

A.3

$$\int_{\Pi} \nabla \cdot (\mathbf{\tau}_\mu \cdot \mathbf{v}) \, dV = I(\phi_1 - \phi_2) - \int_{\Pi} \mathbf{J} \cdot \mathbf{E} \, dV = I(\phi_1 - \phi_2) - P_\Omega \tag{A.16}$$

and the macroscopic balance of the mechanical energy is finally obtained by combining (A.8), (A.9), (A.10) and (A.16):

$$\rho Q(\frac{v_2^2}{2} + \frac{p_2}{\rho}) - \rho Q(\frac{v_1^2}{2} + \frac{p_1}{\rho}) = I(\phi_1 - \phi_2) - P_\Omega - P_\mu \tag{A.17}$$

Thus, the total electrical energy transferred to the cone-jet is partially converted into mechanical energy, and partially degraded by viscous and ohmic dissipation.

The macroscopic balance of the internal energy can be derived by using the first law of thermodynamics for an open system. Conservation of energy in the control volume bounded by the surfaces Σ_0, Σ_1 and Σ_2 requires the net flux of energy (internal, kinetic and surface energy) exiting the control volume to be balanced by the net rate of heat and electrical energy addition, combined with the rate of work done by the stresses on Σ_1 and Σ_2 (pressure work and surface tension work, we again neglect the work done by the viscous stresses):

$$Q(\rho u_2 + \rho \frac{v_2^2}{2} + \frac{2\gamma}{R_2}) - Q(\rho u_1 + \rho \frac{v_1^2}{2} + \frac{2\gamma}{R_1}) = I(\phi_1 - \phi_2) + Q(p_1 - \frac{2\gamma}{R_1}) - Q(p_2 - \frac{2\gamma}{R_2}) + \dot{q} \tag{A.18}$$

u and $\dot{q}$ stand for the internal energy per unit mass and the net rate of heat addition. It is worth noting that in each boundary the flux of surface energy is exactly balanced by the rate of work done by the resultant of the surface tension. The macroscopic balance of mechanical energy can now be subtracted from (A.18) to yield the following macroscopic balance for the fluid's internal energy, and its temperature change

$$u_2 - u_1 = c\,(T_2 - T_1) = \frac{P_\Omega + P_\mu + \dot{q}}{Q\rho} \tag{A.19}$$

c is the heat capacitance per unit mass. The viscous dissipation of mechanical energy and the ohmic dissipation of electrical energy increase the internal energy of the fluid. Furthermore, the heat fluxes across the boundaries of our cone-jets (radiation through Σ_0, and conduction through Σ_1 and Σ_2) are likely negligible.

A.4